ADVANCED FUNCTIONAL MATERIALS
www.afm-journal.de

Polyoxometalate-coupled Graphene via Polymeric Ionic Liquid Linker for Supercapacitors

MinHo Yang, Bong Gill Choi, Sung Chul Jung, Young-Kyu Han, Yun Suk Huh, and Sang Bok Lee**

The integration of electrical double-layer capacitive and pseudocapacitive materials into novel hybrid materials is crucial to realize supercapacitors with high energy and power densities. Here, high levels of energy and power densities are demonstrated in supercapacitors based on a new type of nanohybrid electrode consisting of polyoxometalate (POM)-coupled graphene in which a polymeric ionic liquid (henceforth simply PIL) serves as an interfacial linker. The adoption of PIL in the construction of nanohybrids enables a uniform distribution of discrete POM molecules along with a large surface area of graphene sheets. When testing electrochemical characteristics under a two-electrode system, as-prepared supercapacitors exhibit a high specific capacitance (408 F g^{-1} at 0.5 A g^{-1}), rapid rate capability (92% retention at 10 A g^{-1}), a long cycling life (98% retention during 2000 cycles), and high energy (56 Wh kg^{-1}) and power (52 kW kg^{-1}) densities. First-principles calculations and impedance spectroscopy analysis reveal that the PILs enhance the redox reactions of POMs by providing efficient ion transfer channels and facilitating the charge transfer in the nanohybrids.

1. Introduction

Supercapacitors (SCs), also called electrochemical capacitors, are a promising energy storage device for many portable electronics and hybrid electrical vehicles due to their high power capability, long lifetimes, and rapid charge/discharge rates.[1–3] Although SCs are capable of delivering higher power densities than most batteries, their limited energy density, an order of magnitude lower than that of batteries, makes them only complementary power systems for battery operations.[2] In this regard, recent research has focused on improving the energy density while maintaining the other specifications (e.g., the power density and cycling life). Pseudocapacitive metal oxides (or hydroxides) and conducting polymers have been extensively explored as active materials to store electrical charges through redox (Faradic) reactions on their surfaces.[4] These studies have achieved substantially high pseudocapacitance (300–1200 F g^{-1}) levels which exceed those of electrical double-layer capacitors using carbon-based materials (60–300 F g^{-1}).[5] However, there are significant drawbacks to the use of these pseudocapacitors—capacitance fading at a high rate and long-term cycling due to the intrinsic low electrical conductivity of the metal oxides and the irreversibility of the Faradic reaction.

To address these issues, one of the most promising approaches is the construction of nanostructured composites in which pseudocapacitive materials are combined with carbon materials (particularly carbon nanotubes (CNTs) and graphene) owing to the combination of the attractive qualities of these dissimilar components.[6–12] Pseudocapacitive materials play an important role in surface redox reactions for a large amount of charge storage, while carbon materials enable the more effective utilization of the redox properties of pseudocapacitive materials and enhance the electrochemical performance due to the good electrical conductivity and mechanical properties of the carbon materials.[6] Based on these factors, a large number of hybrid or composite materials, such as RuO_2/CNT,[7] MnO_2/graphene,[8–10] Fe_3O_4/graphene,[11] and $Ni(OH)_2$/graphene[12] have been intensively explored as electrode materials for SCs. These studies have resulted in significant enhancements in energy and power performance compared to the individual components. However, the reported energy (2.3–12.1 Wh kg^{-1}) and power density (390–5695 W kg^{-1}) values of SCs are still low to use as a powering source in prevailing applications in consumer electronics.[13] The main obstacle preventing the

M. Yang, Prof. S. B. Lee
Graduate School of Nanoscience and Technology
Korea Advanced Institute of Science and Technology
Daejeon 305–701, Republic of Korea
E-mail: slee@umd.edu
Prof. B. G. Choi
Department of Chemical Engineering
Kangwon National University
Samcheok 245–711, Republic of Korea
Dr. S. C. Jung, Prof. Y.-K. Han
Department of Energy and Materials Engineering
Dongguk University-Seoul
Seoul 100–715, Republic of Korea
E-mail: ykenergy@dongguk.edu
Prof. Y. S. Huh
Department of Biological Engineering
Inha University
Incheon 402–751, Republic of Korea
Prof. S. B. Lee
Department of Chemistry and Biochemistry
University of Maryland
College Park, MD 20742, USA

DOI: 10.1002/adfm.201401798

realization of the theoretical capacitance is strongly related to the limited ion diffusion within the thick layer of the metal oxide/hydroxide and the poor electron transport through semiconducting or even electron-insulating metal oxides. Moreover, an integration strategy for hybrid materials remains a major challenge with regard to the array density and position of pseudocapacitive materials on carbon supports.

Polyoxometalates (POMs), which are nanoscale transition metal-oxygen clusters, have attracted much attention in recent years as key components in the design of electrode materials for energy storage devices due to their high theoretical values, electron and proton transfer/storage abilities, thermal stability, and lability of their lattice oxygen.[14–19] POMs are highly soluble owing to their anionic nature; as a result, they need to be integrated into hybrid materials for supercapacitor applications.[20–24] Thus far, tremendous efforts have been devoted to immobilizing POMs onto specific supports, including conducting polymers[20–22] and polymer electrolytes[23,24] based on their strong electrostatic interactions. However, the entrapping of POMs into polymer matrices inevitably limits the available redox active sites of the POMs, which can constrain their intrinsic capacitances (e.g., 120 F g^{-1} for POM/polyaniline[20] and 210 F g^{-1} for POM/polypyrrole).[21] In addition, the electrical conductivity values of these materials are not guaranteed. More recently, graphene with its large surface area and high electrical conductivity has been newly proposed as a support for anchoring POMs.[25–27] Although the combination of POM and graphene can increase the electrical conductivity and provide large available active sites, previously reported approaches have difficulties related to the strong integration between POMs and graphene as well as the control of the density and position of POMs.

Herein, we report a rational design and the synthesis of POM ($H_3PMo_{12}O_{40}$)-coupled reduced graphene oxide (RGO) through a simple anion exchange in which a polymeric ionic liquid (henceforth PIL) is employed as a linker to bridge two components. The high density of POMs is individually distributed over the surface of PIL-functionalized RGOs. This type of architecture of the POM/PIL/RGO nanohybrids enables excellent contact, enhancing the redox reactions of the POMs and the charge transfer at the interface, as verified by density functional theory (DFT) calculations and impedance spectroscopic analysis. When testing a two-electrode system using POM-coupled graphene nanohybrids, the supercapacitors exhibit high rate capability and good cycling stability while maintaining a highly reversible capacity and high energy levels and power densities.

2. Result and Discussion

The POM/PIL/RGO nanohybrids were obtained by the functionalization of the RGOs with PILs followed by an anion exchange using POMs (**Figure 1**A). The PIL, poly(1-vinyl-3-ethylimidazolium bromide), was synthesized and used as a functional material for the nanohybrids. The use of the PIL allowed us i) to effectively prevent the aggregation of RGO sheets, ii) to provide uniform deposition sites for POM distribution throughout the PILs, and iii) to enhance the interfacial reactions between the two counterpart components (POM and RGO).[28,29] Graphene oxide (GO) as the starting material was prepared by the chemical exfoliation of commercial graphite, yielding an aqueous suspension. GOs suspended in a water solution were functionalized by PILs and were then reduced using a hydrazine solution. Cation–π interactions between the PIL and the RGO during the reduction process[30] led to a PIL/RGO complex which was easily re-dispersed in water through gentle sonication (Figure S1, Supporting Information). The PIL/RGO complex had a thin layered and wrinkled flake-like structure (Figure 1B). The functionalization of PILs improved a surface area of 248 m^2 g^{-1} compared to the pristine RGO (96 m^2 g^{-1} in Supporting Information). After removal of unbound PIL, the POM solution was added into the PIL/RGO suspension. Br^- anions on the PIL/RGO were easily exchanged with POM anions, thereby producing uniformly distributed POM/PIL/RGO nanohybrids (Figure 1A). The halide anions (e.g., Cl^- and Br^-) of ionic liquid can be readily exchanged by POM anions (larger available negative charge) through metathesis reaction or conversion into complex anions by Lewis acid addition.[31]

Examination by transmission electron microscopy (TEM) revealed the formation of uniformly distributed and discrete POM molecules anchored onto the surfaces of the PIL/RGO sheets (Figure 1C,D). The average size of the POM, estimated based on the high-resolution TEM image shown in Figure 1D, was about 1.5 nm, which corresponds to the molecular size of $[PMo_{12}O_{40}]^{3-}$.[32] Element mapping measurements by energy dispersive X-ray spectroscopy were also conducted on the same sample image in Figure 1C (Figure 1E). The molybdenum and oxygen signals of the POM and the nitrogen signal of the PIL uniformly overlapped, which is indicative of a uniform distribution of POM molecules over the entire PIL/RGO surface. In contrast, the control sample of POM/RGO without PIL functionalization exhibited the partial deposition of POMs under experimental conditions identical to those of the POM/PIL/RGO (Figure S2). Using inductively coupled plasma-atomic emission spectrometer (ICP-AES) measurements, we estimated the mass content of the POMs in the composites at approximately 38.4 wt% for POM/PIL/RGO and 6.2 wt% for POM/RGO. The PILs offered clearly more binding sites and led to a uniform distribution of the POMs. The composition ratio of POM/PIL/RGO was estimated from thermogravimetric analysis (TGA) and ICP-AES results; 38.4 wt% for POM, 15.0 wt% for PIL, and 46.6 wt% for RGO (Supporting Information Figure S3 and Table S2).

An anion exchange between the POMs and the Br anions of PIL is the key factor for creating a well-defined morphology of POM/PIL/RGO nanohybrids. This was confirmed by Fourier transform infrared (FT-IR) spectroscopy and X-ray photoelectron spectroscopy (XPS) measurements before and after chemical reduction and anion exchange reactions (**Figure 2** and Supporting Information Figure S4, respectively). The characteristic bands of the GO sheets were observed at 1722 cm^{-1} (C=O), 1620 cm^{-1} (aromatic C=C), 1366 cm^{-1} (C–OH), 1223 cm^{-1} (C–O–C), and 1048 cm^{-1} (C–O–C in epoxide).[33] After chemical reduction, the peak intensities of the oxygen-containing groups for PIL/RGO were significantly decreased as a consequence of the deoxygenation process.[33] In addition, the wave number shift which is corresponded to C=C and C–N ring

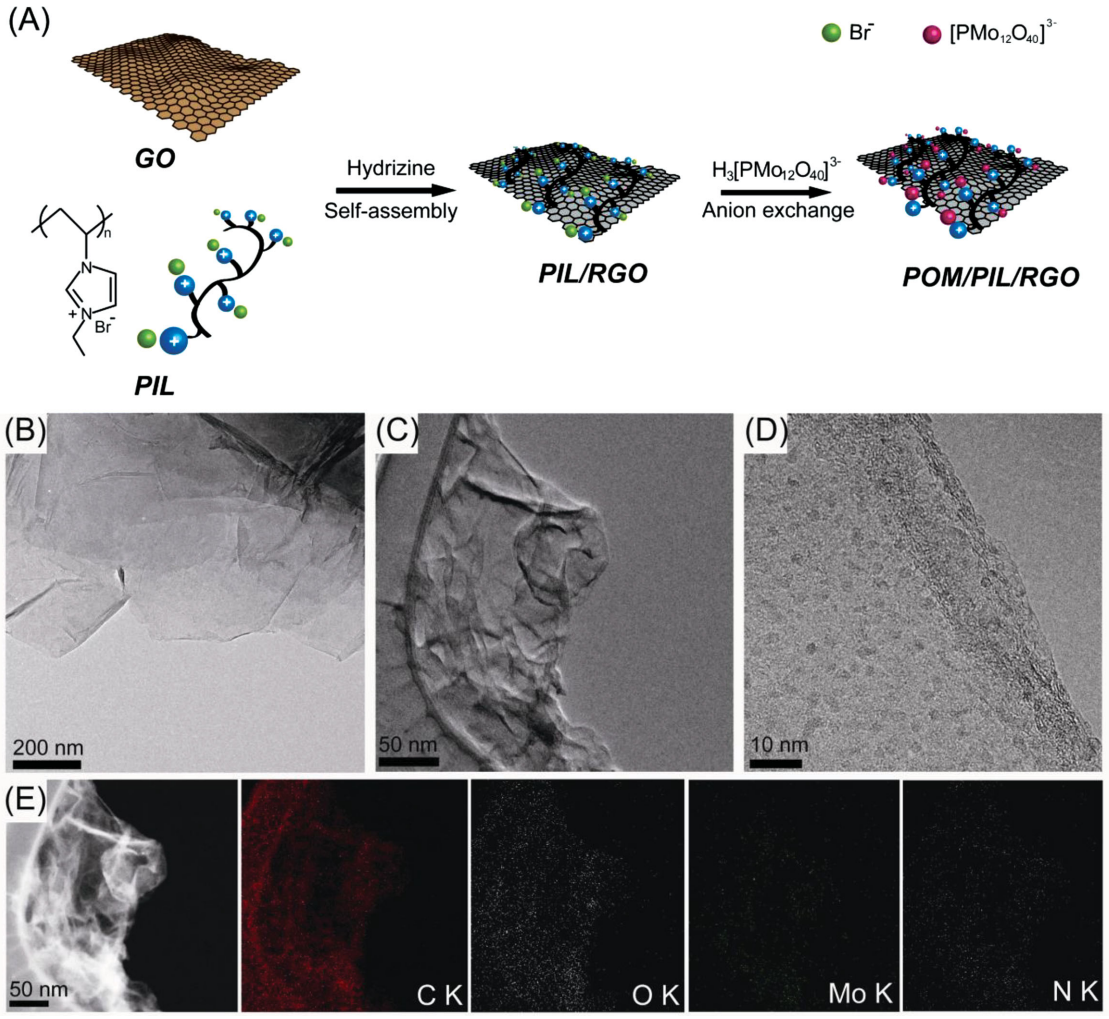

Figure 1. A) Schematic illustration of the synthetic process for the POM/PIL/RGO nanohybrids via self-assembly and anion exchange reaction. TEM images of B) PIL/RGO and C,D) POM/PIL/RGO. E) HADDF-TEM image of POM/PIL/RGO and 2D elemental mapping for the detected four elements; C, O, Mo, and N, respectively.

stretching vibration in imidazolium ring (at around 1568 cm^{-1} and 1158 cm^{-1}, respectively) indicated non-covalent functionalization of RGO with PILs.[30] Compared to PIL/RGO, new characteristic peaks at 1065 cm^{-1} (P–O_a), 962 cm^{-1} (M=O_d), 870 cm^{-1} (Mo–O_b–Mo), and 782 cm^{-1} (Mo–O_c–Mo) clearly appeared in the POM/PIL/RGO sample, in good agreement with previously reported data.[34] These observations indicated that the grafting of POM molecules onto PIL/RGO sheets was successfully achieved by an anion exchange reaction. An XPS analysis further confirmed that the bromide anion was completely replaced by the $[PMo_{12}O_{40}]$ anion through the anion exchange process. After grafting POM molecules onto the PIL/RGO, the Br 3d signals at 67.8 eV completely disappeared, while the Mo 3d signal at 233.2 eV was observed at the POM/PIL/RGO (Figure S4, Supporting Information). Our DFT calculations also revealed that the anion exchange reaction is energetically favorable; specifically, the reaction $[C_7H_{11}N_2]^+Br^- + H_3PMo_{12}O_{40} \rightarrow [C_7H_{11}N_2]^+[H_2PMo_{12}O_{40}]^- + HBr$ on graphene is exothermic by 16.1 kcal mol^{-1} (Figure S5, Supporting Information).

In order to investigate the electrochemical characteristics of the PIL/POM/RGO, a three-electrode system consisting of a working electrode of PIL/POM/RGO, a counter electrode of Pt wire, and a reference electrode of Ag/AgCl electrode was tested in 0.5 M H_2SO_4. POM/PIL and POM/RGO were also tested as control samples under identical conditions. Notably, POMs are known as an electron sponge,[15] as they can theoretically accumulate eight electrons at their bonding molecular orbitals when in the form of delocalized POMs and can facilitate proton transfers along the surface of the spherical POM molecules due to the delocalization of the surface charge.[35,36] The cyclic voltammogram (CV) of POM/PIL/RGO represents three sharp and well-defined redox peaks (**Figure 3**A). The area under the current–voltage curve for the POM/PIL/RGO is much greater than those of POM/RGO and POM/PIL, indicating its superior capacitive performance. In contrast, POM/RGO exhibits a nearly rectangular shape with weak redox waves due to the dominant contribution of charging current of RGOs (Figure 3A). This result demonstrates that the PILs on the RGOs provided amount of binding sites to anchor POMs, which result in

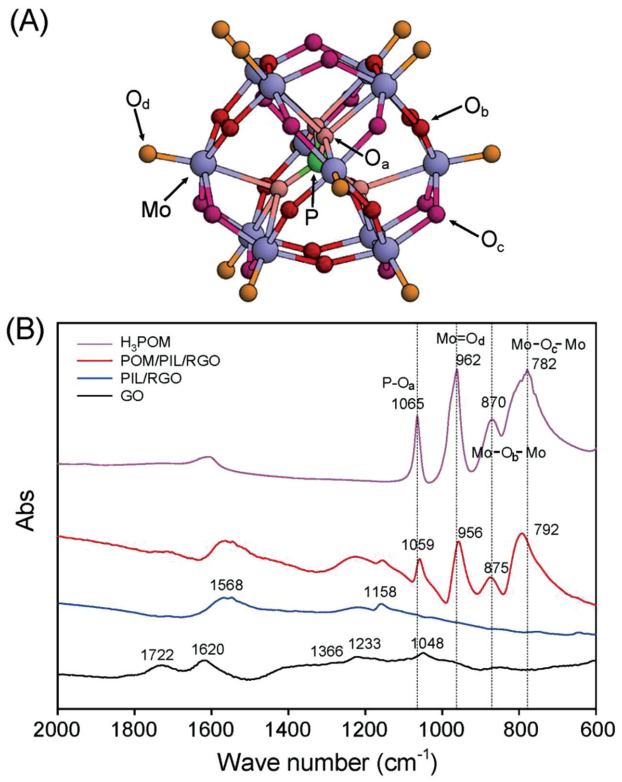

Figure 2. A) Keggin-type phosphomolybdate $[PMo_{12}O_{40}]^{3-}$, one of representative POMs, consisting of twelve MoO_6 octahedrons surrounding a central PO_4 tetrahedron. There are three types of O atoms: four central unreactive O atoms (O_a), twenty-four bridging O atoms that connect two Mo atoms (O_b and O_c), and twelve terminal O atoms bonded to one Mo atom (O_d). The O_b and O_c sites have different Mo–O–Mo bond angles of 152° and 126°, respectively. B) FT-IR spectra of GO, PIL/RGO, POM/PIL/RGO, and H_3POM.

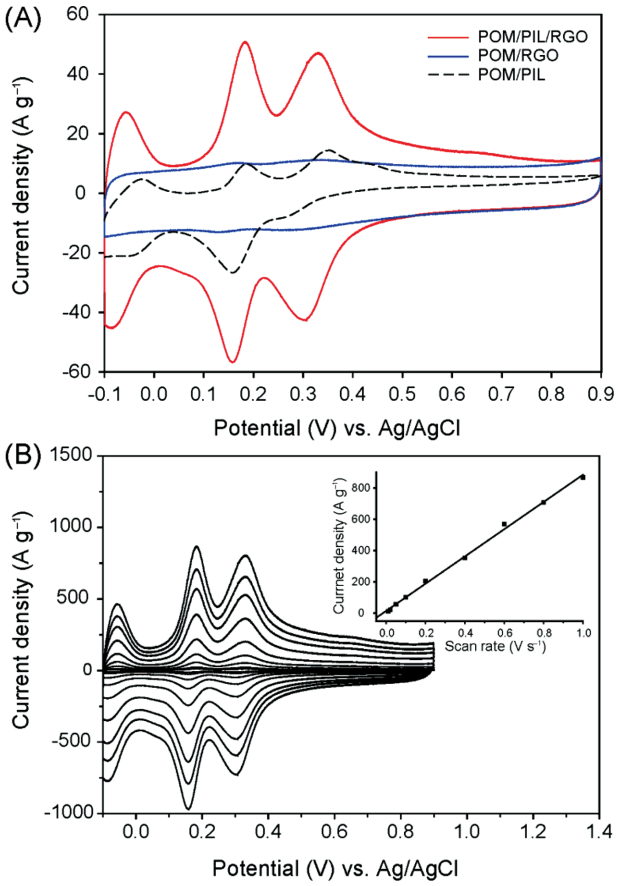

Figure 3. A) CVs of POM/PIL/RGO, POM/RGO, and POM/PIL electrodes with 0.5 M H_2SO_4 aqueous solution at scan rate of 50 mV s^{-1}. B) CV of POM/PIL/RGO at different scan rates of 0.01, 0.02, 0.05, 0.1, 0.2, 0.4, 0.6, 0.8, 1.0 V s^{-1} (from inner to outer); Inset is a plot of the peak current of the second oxidation wave as a function of scan rate.

good electrochemical reactions. As a result, PIL contents influenced the capacitive behavior of the POM/PIL/RGO electrode (Figure S6). From this data, the optimized composition of PIL in POM/PIL/RGO nanohybrids was chosen to be ≈15 wt%. The specific capacitances of POM/PIL/RGO electrode were evaluated with CV and galvanostatic charge/discharge curves (Supporting Information Figure S7 and Table S3). The maximum specific capacitance of 456 F g^{-1} for POM/PIL/RGO electrode was obtained at scan rate of 10 mV s^{-1}, which is two-fold higher than that of POM/RGO electrode (181 F g^{-1}). The results of POM/PIL/RGO and POM/RGO electrodes obtained from CV were consistent with galvanostatic cycling.

Moreover, as the scan rates increased to 1000 mV s^{-1}, the peak current densities for the POM/PIL/RGO increased linearly (vs the scan rates, as shown in Figure 3B). This observation suggests that the POM molecules immobilized on the surface of RGO undergoes a surface confined redox process and fast ion diffusion for the redox reactions into the electrode surface, which implies excellent rate capability. Based on the redox peaks of the POM/PIL/RGO, their peak separations (ΔE_p) were calculated to be as small as ≈23–26 mV. Interestingly, the number of electrons involved in each of the first, second, and third redox reactions (as calculated from ΔE_p) was ≈2.4, which may have resulted from electron delocalization in PIL-bridged POM/RGO nanohybrid systems. This value for POM/PIL/RGO is, to the best of our knowledge, higher than those of previously studied POM-based composites (two electron and two-proton mechanism).[37]

To realize our nanohybrids as an electrode material in SCs, a symmetric SC device was fabricated by a two-electrode system. **Figure 4**A presents the typical galvanostatic charging/discharging behavior of the POM/PIL/RGO-based SCs (POM/PIL/RGO-SCs) in a 0.5 M H_2SO_4 electrolyte solution. Prominent redox waves are clearly observed for the POM/PIL/RGO-SCs, which is consistent with the CV curves in Figure 3A. The specific capacitance of the POM/PIL/RGO-SCs and POM/RGO-SCs were calculated from the discharge curve and plotted with respect to current densities ranging from 0.5 to 10 A g^{-1} (Figure 4B). The maximum capacitance value of the POM/PIL/RGO-SCs (408 F g^{-1}) was obtained at a constant current density of 0.5 A g^{-1}, which was two-fold higher than that of the POM/RGO-SCs (162 F g^{-1}). This value retained 92% of its initial value with an increase in the operation rate to 10 A g^{-1}. In contrast, the capacitance of the POM/RGO-SCs decreased significantly as the constant current density increased, falling to a value of 110 F g^{-1} with 67% retention. Note that the maximum specific capacitance value of POM/PIL/RGO was higher than those

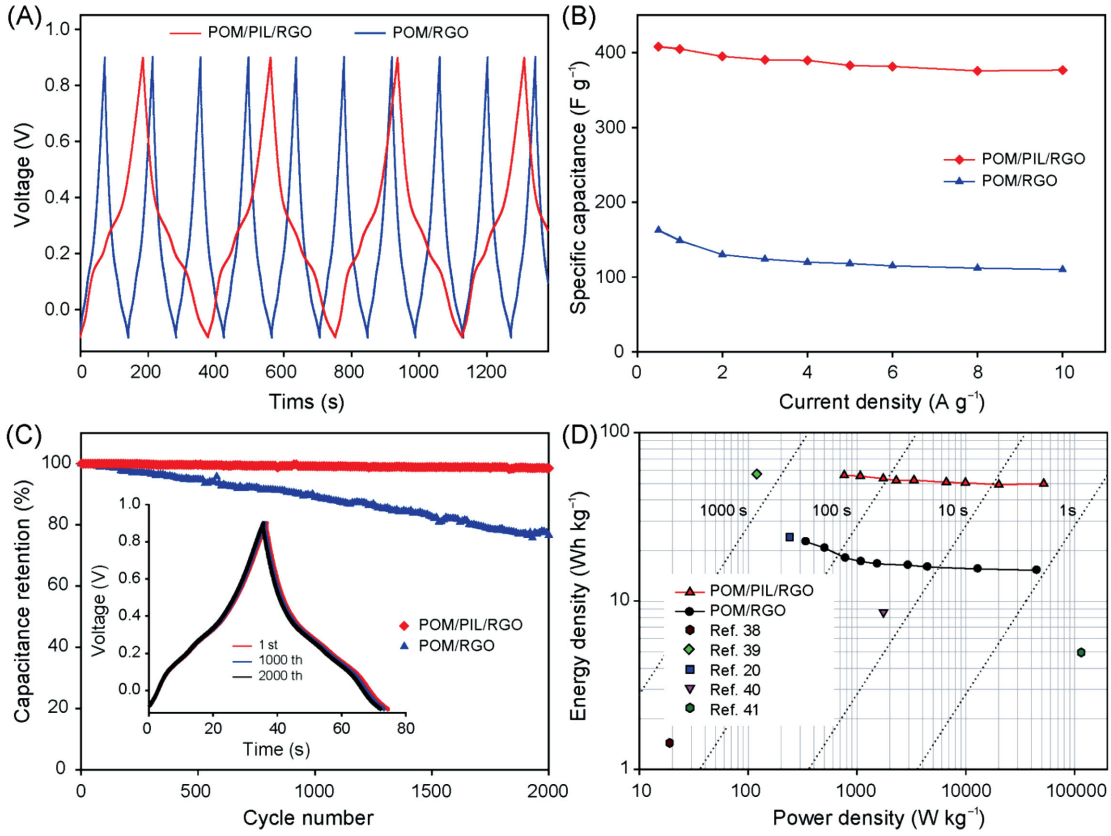

Figure 4. A) Galvanostatic charge/discharge curves of POM/PIL/RGO and POM/RGO at current density of 2 A g^{-1}; B) Specific capacitances calculated from galvanostatic charge/discharge with various current densities; C) Capacitance retention of the POM/PIL/RGO and POM/RGO electrode evaluated at a constant charge/discharge cycling rate of 10 A g^{-1}; D) A Ragone plot related to energy and power densities of supercapacitors based on the POM/PIL/RGO electrode, compared with the other supercapacitors systems using POM.

of other previously reported graphene/metal oxide nanocomposites, including 380 F g^{-1} for graphene/MnO_2/PEDOT:PSS at 0.5 mA g^{-1},[9] 216 F g^{-1} for MnO_2/CMG_{15} at 150 mA g^{-1},[10] 326 F g^{-1} for e-Fe_3O_4@RGO at 0.5 A g^{-1},[11] and 166 F g^{-1} for $Ni(OH)_2$/UFG at 0.5 A g^{-1}.[12]

The long cycle life of SCs is one of the most important factors with regard to their practical applications. To demonstrate the cycling stability clearly, our POM/PIL/RGO-SCs were tested with more than 2000 galvanostatic charge/discharge cycles even at a high rate of 10 A g^{-1} (Figure 4C). We found as high as 98% retention of the initial specific capacitance for POM/PIL/RGO-SCs, indicating good cycling performance. In addition, highly reversible capacitive behaviors were observed, with the charge/discharge curves of the first, 1000th, and 2000th cycles nearly overlapping (as shown in the inset of Figure 4C). The structural preservation of POM/PIL/RGO electrode was visually confirmed by scanning electron microscopy (SEM) images before and after 2000 cycles (Figure S8, Supporting Information). In addition, a negligible leaching of POMs was observed at POM/PIL/RGO electrode (Table S4, Supporting Information). These results indicate excellent structual stability of POM/PIL/RGO electrode. Under this harsh condition, the POM/RGO-SCs exhibited inferior cycling stability, with 77% retention of their original capacitance after 2000 cycles. Thus, the incorporation of PIL not only significantly enhances the specific capacitance levels of the nanohybrids but also improves their cyclic stability due to the intrinsic properties of the PIL and the synergistic effect of the nanohybrids.[29]

Moreover, our POM/PIL/RGO-SCs exhibit high levels of energy and power densities. A Ragone plot of the corresponding specific energy versus power values was investigated and compared with other reported POM-based SCs (Figure 4D). In general, an increase in the power density comes at a cost to the energy density value. Remarkably, the POM/PIL/RGO-SCs showed no significant decrease in the energy density upon an increase in the power density. A maximum energy density of 56 Wh kg^{-1} (with a power density of 0.8 kW kg^{-1}) and a maximum power density of 52 kW kg^{-1} (with an energy density of 50 Wh kg^{-1}) were obtained from SCs based on two symmetric POM/PIL/RGO electrodes with an operating voltage of 1.0 V. These values are superior compared to presently available SCs and other POM-based symmetrical supercapacitors, including POM/polypyrrole (PPy)//POM/PPy (1.44 Wh kg^{-1} at 18.90 W kg^{-1}),[38] POM/MWNT//POM/MWNT (57 Wh kg^{-1} at 120 W kg^{-1}),[39] POM/polyaniline (PANI)//POM/PANI (24 Wh kg^{-1} at 240 W kg^{-1}),[20] POM/ionic liquid (IL)//POM/IL (8.6 Wh kg^{-1} at 1.75 kW kg^{-1}),[40] and POM/activated carbon (AC)//POM/AC (4.96 Wh kg^{-1} at 115 kW kg^{-1}).[41]

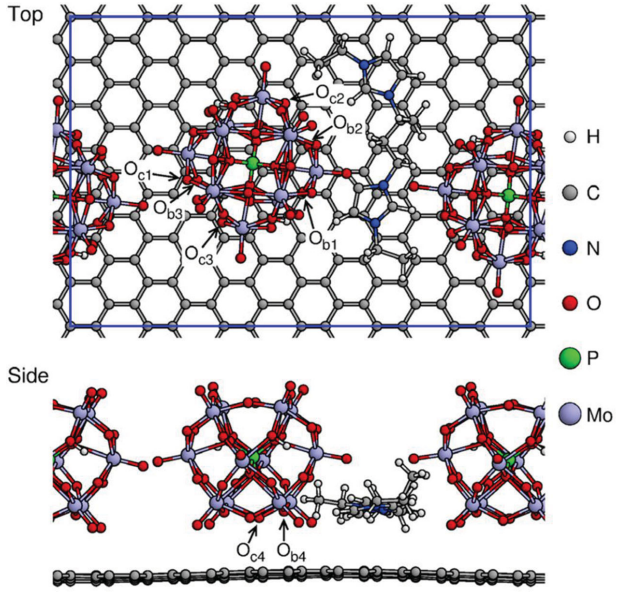

Figure 5. Optimized PIL/POM (2[$H_2PMo_{12}O_{40}$][$C_{14}H_{24}N_4$]) structure on graphene. In the center $H_2PMo_{12}O_{40}$, eight different O_b and O_c sites for H adsorption are indicated by arrows. Solid lines represent the used periodic unit cell. We note that the O_{b4} and O_{c4} sites are available as H adsorption sites despite the O sites are close to graphene (see the adsorption energies in Figure 6).

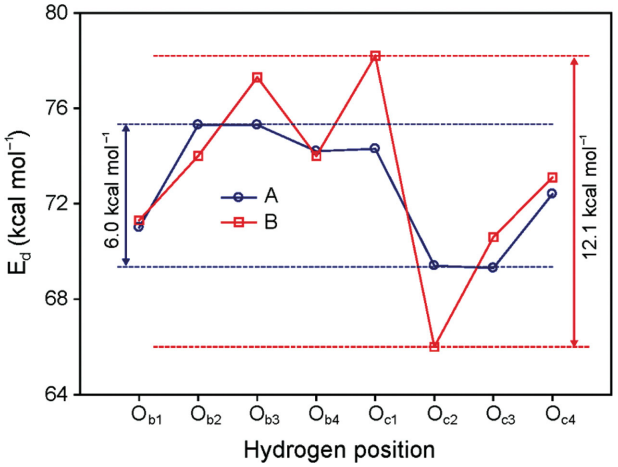

Figure 6. Adsorption energies E_d of a single H atom on eight different O_b and O_c sites of A) $H_2PMo_{12}O_{40}$/graphene and B) 2[$H_2PMo_{12}O_{40}$][$C_{14}H_{24}N_4$]/graphene. The adsorption sites are shown in Figure 5.

As compared to aqueous electrolytes, the POM/PIL/RGO-SCs were further investigated using 0.5 M $LiClO_4$ in acetonitrile (Figure S9, Supporting Information). The POM/PIL/RGO-SCs were cycled from 0 V to 2 V at constant current density of 1 A g^{-1}. The energy and power densities of the POM/PIL/RGO-SCs were estimated to be 147 Wh kg^{-1} and 1.23 kW kg^{-1}, respectively.

DFT calculations further explain the origin of the highly enhanced redox reactions of the POM/PIL/RGO nanohybrids. To describe the dispersion interactions correctly, the van der Waals density functional (vdW-DF) for the non-local correlation part was employed in the DFT calculations.[42,43] **Figure 5** shows the most stable POM/PIL/graphene structure, where two POMs and one IL dimer (i.e., 2[$H_2PMo_{12}O_{40}$][$C_{14}H_{24}N_4$]), are included in a periodic unit cell. The optimized configuration, in which the two POMs are on opposite sides of the PIL, was found to be more stable by 5.5 kcal mol^{-1} than a configuration with POMs on the same side of PIL (Figure S10, Supporting Information). In order to understand the role of PIL and the neighboring POM in the proton transfer process, we examined the adsorptions of a single H atom on eight different O_b and O_c sites of POM (Figure 5). The calculated adsorption energies are compared with those obtained for the H adsorptions on the same O sites of an isolated POM ($H_2PMo_{12}O_{40}$) on graphene (**Figure 6**). The POM/PIL/graphene system shows a wider range (6.0 → 12.0 kcal mol^{-1}) of H adsorption energies than the isolated POM/graphene system.

These DFT results suggest that the H adsorption energetics on a POM in the POM/PIL nanohybrids is significantly affected by adjacent PILs and POMs. From an electrostatic standpoint, the PIL cations and the POM anions suppress and facilitate the proton adsorption reaction, respectively, on the adjacent POM. For instance, the H atom on the O_{c2} site interacts repulsively with the neighboring PIL cation and thus has lower adsorption energy by 3.4 kcal mol^{-1} than that of the H atom without neighboring PILs. On the other hand, the H atom on the O_{c1} site is attracted to the adjacent POM anion and has higher adsorption energy than the H atom without adjacent POMs by 3.8 kcal mol^{-1}. The interplay between the PILs and the POMs appears to provide new reactive channels that enable efficient proton transfers during both the charging and discharging process. Thus, it is evident that the PIL-grafted POMs greatly enhance the ability of redox reactions on graphene.

Furthermore, we found clear evidence of an improved charge transfer in POM/PIL/RGO compared to the POM/RGO from an electrochemical impedance spectroscopic analysis (**Figure 7**). In the Nyquist plots shown in Figure 7A, the charge transfer resistance (R_{ct}) values were calculated using equivalent circuits: 1.69 Ω for POM/PIL/RGO and 4.24 Ω for POM/RGO. This lower value likely stems from the significant role of the PILs in facilitating the charge transfer at the interface between the RGO and the POM. Figure 7B displays a plot of the normalized imaginary-part $|Q|/|S|$ and real-part $|P|/|S|$ complex power as a function of the frequency (f_0). The value of the complex power ($S(\omega)$) is the apparent power; it can be expressed as[44]

$$S(\omega) = P(\omega) + iQ(\omega)$$

where $P(\omega)$ and $Q(\omega)$ are correspondingly the active and reactive power obtained from the real and imaginary parts of the capacitance, respectively. The crossing of the two plots appears when $|P| = |Q|$, corresponding to the relaxation time constant τ_0 ($= 1/2\pi f_0$) which defines the transition from resistive to capacitive behavior. The relaxation time constant was calculated to be ≈12.7 ms for the POM/PIL/RGO, which is four-fold lower than that of POM/RGO (≈50.4 ms). This result clearly demonstrates that POM/PIL/RGO has much faster capacitive behavior compared to POM/RGO in the low-frequency region.

The attractive electrochemical performance of POM/PIL/RGO is attributed to the interfacially driven nanohybrid structures. In particular, the PILs serve multifunctionalities at the

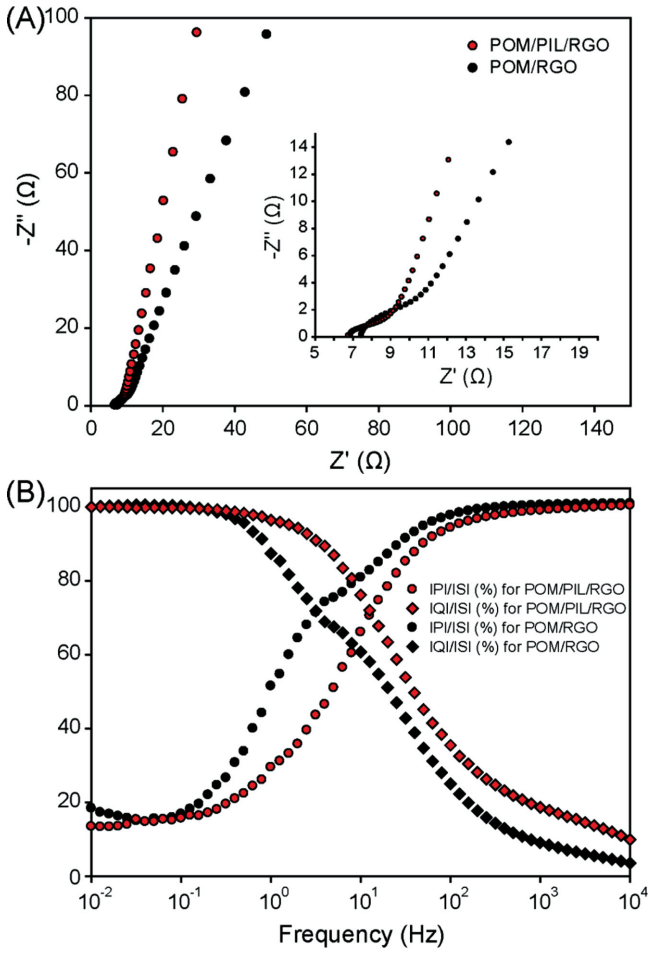

Figure 7. A) Nyquist plots of the POM/PIL/RGO and POM/RGO electrode obtained over the frequency range of 100 kHz to 10 mHz by applying a sine wave with an amplitude of 10 mV (magnified figure at the high frequency, inset); B) Plots of normalized reactive power |Q|/|S| and reactive power |P|/|S| as a function of frequency.

interface between the POMs and the RGO sheets. The functionalization of PIL on the surface of RGO sheets increased a surface area (Table S1, Supporting Information), and thus provided a large amount of binding sites for deposition of POMs on PIL/RGOs. The high ionic conductivity of PIL enabled rapid and efficient ion transfer channels on POM/PIL/RGOs, which can facilitate redox reactions of POMs, as demonstrated by DFT results. In addition, compared to the POM/RGO, POM/PIL/RGO had a shorter ion diffusion length, therby leading to the enhanced charge transfer behavior at the interface between electrode and electrolyte (Impedance analysis, Figure 7). Hence, the enhanced high-rate capability of the POM/PIL/RGO electrodes can be understood by their nanohybrid structure of POM-coupled PIL/RGO sheets. Moreover, long cycle life (98% retention over 2000 cycles) of POM/PIL/RGO-SCs is strongly associated with an excellent strucural stability of POM/PIL/RGOs, as verified by morphology change and leakage test of POMs after 2000 cylces (Figure S8 and Table S4, Supporting Information). Consequnetly, such superior nanohybrid structure of POM-coupled PIL/RGO sheets led to the high levels of energy and power densities of supercapacitors.

3. Conclusion

We developed a simple and effective strategy for the nanohybridization of POM clusters and RGO sheets using PILs as an interfacial linker. The resulting materials were employed as electrode materials for high-performance SCs. The adoption of an anion exchange mechanism between POMs and the anion groups of PILs ensured that the POMs were uniformly distributed over the high surface area of the RGOs. In consequence, the POM/PIL/RGO electrodes exhibited significantly improved electrochemical performance levels compared to the POM/RGO electrodes, including high energy and power densities while maintaining good cycling stability on full-cell tests. The DFT calculations and impedance spectroscopy results demonstrated that the unique intermolecular structure of POM/PIL/RGO enhanced the reversible redox reactions of POMs and the interfacial charge transport. Our interfacial engineering approach at the nanoscale is a promising method for the creation of a finely controlled structure and to ensure a heterogeneous nanomaterial composition that can significantly improve the electrochemical performance of energy storage devices.

4. Experimental Section

Synthesis of the Polymeric Ionic Liquid: The PIL, poly(1-vinyl-3-ethylimidazolium bromide) ([VEIM][Br]), was synthesized according to a previously reported procedure.[45,46] A mixture of [VEIM][Br] (1.5 g), 2,2′-Azobis(isobutyronitrile) (AIBN, 7.5 mg) and 15 mL of methanol was added into a three-necked flask in a preheated oil bath set at 60 °C with stirring under a nitrogen atmosphere. After 18 hours, the reaction mixture was cooled to room temperature, and a precipitate formed in ethyl ether. Residue monomers were removed by dialysis in water. The solution was concentrated with a rotavapor, and the final product was dried under a vacuum at room temperature. The purity of the PIL (for an average molecular weight of ≈26 000)[46] was checked by ^{1}H NMR spectroscopy (see Figure S11 in the Supporting Information).

Preparation of the POM/PIL/RGO Nanohybrids: As starting materials, graphene oxide (GO) was prepared by a modified Hummers method.[47] The PIL/RGO was prepared by dispersing the as-obtained GO (5 mg) and PIL (10 mg) in de-ionized (DI) water (20 mL) by sonication for 60 min and then mixing it with hydrazine (100 µL) at 85 °C for 24 h. The resulting mixture was then washed and filtered to yield PIL/RGO nanohybrids. POM/PIL/RGO was prepared by vigorously stirring an aqueous solution of PIL/RGO and excess phosphomolybdic acid hydrate ($H_3[PMo_{12}O_{40}]\cdot xH_2O$) overnight. POM/PIL/RGO was collected by filtration and thoroughly washed with water to remove any unbound POM.

Material Characterization: High-resolution TEM images were obtained using a field-emission TEM (JEM2100F, JEOL Ltd.) operated at 200 kV. SEM images were obtained using a field emission scanning electron microscope (S-4800). The FT-IR spectra were collected on a JASCO FT-IR 470 plus instrument. Each spectrum was recorded from 4000 to 400 cm^{-1} using 12 scans at a resolution of 4 cm^{-1}. XPS data were obtained using a Thermo MultiLab 2000 system. An Al Mgα X-ray source at 200 W was used with pass energy of 20 eV and a 45° takeoff angle in a 10^{-7} Torr vacuum analysis chamber. An elemental analysis of Mo in the solid sample was carried out by an inductively coupled plasma optical emission spectrometry analysis under standard conditions (iCAP 6300, Thermo Scientific). TGA was performed on a TGA 92–18 (Setaram) using a heating rate of 10 °C min^{-1}. N_2 adsorption/desorption was determined by Brunauer-Emmett-Teller (BET) measurements using an ASAP-2010 surface area analyzer. The BET method was used to calculate the specific surface area of samples. The ^{1}H NMR spectra were recorded a Bruker AV400 400 MHz spectrometer using D_2O as a solvent.

Electrochemical Measurements: The All of electrochemical experiments were conducted on a VersaSTAT 4 (Princeton Applied Research). The working electrode, composed of a slurry of 95 wt% active material (POM/PIL/RGO or POM/RGO) and 5 wt% poly(vinylidene difluoride), was coated onto a pretreated stainless steel foil current collector (≈2.0 mg cm^{-2}) and then dried at 60 °C overnight in a vacuum oven. Before used as a current collector, the stainless steel foil was rinsed in an ultrasonic bath of a solution of 0.5 M H_2SO_4 for 10 min and then washed with acetone followed by DI water for 10 min. A Pt wire was used as the counter electrode and an Ag/AgCl electrode was used as the reference electrode. The working electrodes were tested by CV and galvanostatic charge/discharge cycling with a three-electrode cell in 0.5 M H_2SO_4 or 0.5 M $LiClO_4$/acetonitrile as electrolytes. The specific capacitance was estimated from the CV and galvanostatic discharge curves according to the equations: $C_s = \int I dV/(m\nu\Delta V)$ and $C_s = (I\Delta t)/(m\Delta V)$, where $\int I dV$ is the integrating area of CV curves, m is the mass of active materials, ν is the scan rate, ΔV is the potential window, I is the discharge current, and Δt is the discharge time. As for the fabrication of the two-electrode symmetric SC systems, two electrodes with same loading mass were separated by filtrate paper soaked with 0.5 M H_2SO_4 or 0.5 M $LiClO_4$/acetonitrile as electrolyte, and were then sandwiched between two PTFE sheets. The electrochemical impedance spectroscopy measurements were performed over a frequency range from 10^5 to 10^{-2} Hz at sinus amplitude of 10 mV. A cycling test was performed using galvanostatic charge/discharge measurements at a current density of 10 A g^{-1} for 2000 cycles. The specific capacitance derived from the galvanostatic discharge curves was calculated based on the following equation: $C = 4(I\Delta t)/(m\Delta V)$, where I is the discharge current, Δt is the time for a full discharge, m is the total mass of the electrode, and ΔV represents the voltage change during the discharge process.[48] The energy density (E) and power density (P) of the supercapacitors depicted in the Ragone plots were calculated using the equations $E = 1/2C(\Delta V)^2$ and $P = (\Delta V)^2/4RM$, respectively, where C is the specific capacitance, ΔV is the cell voltage after IR drop, R is internal resistance (IR) drop, and M is the total weight of two electrodes.[6]

Computational Details: Density functional theory calculations were carried out using the Vienna Ab initio Simulation Package (VASP).[49] We employed the revised Perdew–Burke–Ernzerhof (revPBE) exchange and correlation functional[50,51] with the introduction of vdW-DF[43,44] for the non-local correlation part to account for the dispersion interactions correctly. The projector augmented wave (PAW) method was used for the ion-electron interaction.[52] The electronic wave functions were expanded in a plane-wave basis set with an energy cutoff of 400 eV. A periodic supercell geometry was employed to model the POM/PIL/graphene system; the cell sizes used were $17.28 \times 17.10 \times 21.00$ Å^3 and $17.28 \times 25.65 \times 21.00$ Å^3 for the anion exchange reaction and the H adsorption on the POM, respectively. One k point was used for the Brillouin-zone integrations. We found that the calculated bond lengths and angles for $[PMo_{12}O_{40}]^{3-}$ are in good agreement with the experimental values within 0.04 Å and 1°, respectively (Table S5, Supporting Information).[53]

Supporting Information

Supporting Information is available from the Wiley Online Library or from the author.

Acknowledgements

M.Y. and B.G.C. contributed equally to this work. Y.-K.H. acknowledge the financial support by the National Research Foundation of Korea Grant funded by the Korean Government (MEST, NRF-2010-C1AAA001–0029018), the Energy Efficiency & Resources Core Technology Program of the KETEP granted financial resource from the MOTIE (No. 20132020000260 and 20132020000340), the IT R&D program (10041856) of MOTIE and the Korea Institute of Energy Research (KIER) grant (B4–2413–02). SBL was supported (electrochemical analysis, mechanism and discussions) as part of the Nanostructures for Electrical Energy Storage (NEES), an Energy Frontier Research Center funded by the US Department of Energy, Office of Science, Office of Basic Energy Sciences under Award Number DESC0001160.

Received: June 3, 2014
Revised: July 22, 2014
Published online: September 11, 2014

[1] P. Simon, Y. Gogotsi, *Nat. Mater.* **2008**, *7*, 845.
[2] Q. Lu, J. G. Chen, J. Q. Xiao, *Angew. Chem. Int. Ed.* **2013**, *52*, 1882.
[3] J. M. Miller, *Ultracapacitor Applications*, The Institution of Engineering and Technology, London **2011**.
[4] B. W. Conway, *Electrochemical Supercapacitors: Scientific Fundamentals and Technological Applications*, Kluwer Academic/Plenum, New York **1999**.
[5] K. Naoi, P. Simon, *Electrochem. Soc. Interface* **2008**, *17*, 34.
[6] S.-K. Kim, Y. K. Kim, H. Lee, S. B. Lee, H. S. Park, *Chem. Sus. Chem.* **2014**, *7*, 1094.
[7] R.-R. Bi, X.-L. Wu, F.-F. Cao, L.-Y. Jiang, Y.-G. Guo, L.-J. Wan, *J. Phys. Chem. C* **2010**, *114*, 2448.
[8] B. G. Choi, Y. S. Huh, W. H. Hong, H. J. Kim, H. S. Park, *Nanoscale* **2012**, *4*, 5394.
[9] G. Yu, L. Hu, N. Liu, H. Wang, M. Vosgueritchian, Y. Yang, Y. Cui, Z. Bao, *Nano Lett.* **2011**, *11*, 4438.
[10] S. Chen, J. Zhu, X. Wu, Q. Han, X. Wang, *ACS Nano* **2010**, *4*, 2822.
[11] Q. Qu, S. Yang, X. Feng, *Adv. Mater.* **2011**, *23*, 5574.
[12] J. Ji, L. L. Zhang, H. Ji, Y. Li, X. Zhao, X. Bai, X. Fan, F. Zhang, R. S. Ruoff, *ACS Nano* **2013**, *7*, 6237.
[13] M. Conte, *Fuel Cells* **2010**, *10*, 806.
[14] D. Ma, L. Liang, W. Chen, H. Liu, Y.-F. Song, *Adv. Funct. Mater.* **2013**, *23*, 6100.
[15] H. Wang, S. Hamanaka, Y. Nishimoto, S. Irle, T. Yokoyama, H. Yoshikawa, K. Awaga, *J. Am. Chem. Soc.* **2012**, *134*, 4918.
[16] F. M. Toma, A. Sartorel, M. Iurlo, M. Carraro, P. Parisse, C. Maccato, S. Rapino, B. R. Gonzalez, H. Amenitsch, T. D. Ros, L. Casalis, A. Goldoni, M. Marcaccio, G. Scorrano, G. Scoles, F. Paolucci, M. Prato, M. Bonchio, *Nat. Chem.* **2010**, *2*, 826.
[17] M. D. Symes, L. Cronin, *Nat. Chem.* **2013**, *5*, 403.
[18] W. Liu, W. Mu, M. Liu, X. Zhang, H. Cai, Y. Deng, *Nat. Commun.* **2014**, *5*, 3208.
[19] S.-M. Wang, L. Liu, W.-L. Chen, Z.-M. Zhang, Z.-M. Su, E.-B. Wang, *J. Mater. Chem. A* **2013**, *1*, 216.
[20] A. K. Cuentas-Gallegos, M. Lira-Cantú, N. Casañ-Pastor, P. Gómez-Romero, *Adv. Funct. Mater.* **2005**, *15*, 1125.
[21] G. M. Suppes, B. A. Deore, M. S. Freund, *Langmuir* **2008**, *24*, 1064.
[22] P. Gomez-Romero, *Adv. Mater.* **2001**, *13*, 163.
[23] Y.-F. Song, R. Tsunashima, *Chem. Soc. Rev.* **2012**, *41*, 7384.
[24] T. Akter, K. Hu, K. Lian, *Electrochim. Acta* **2011**, *56*, 4966.
[25] D. Zhou, B.-H. Han, *Adv. Funct. Mater.* **2010**, *20*, 2717.
[26] R. Liu, S. Li, X. Yu, G. Zhang, S. Zhang, J. Yao, B. Keita, L. Nadjo, L. Zhi, *Small* **2012**, *8*, 1398.
[27] S. Wang, H. Li, S. Li, F. Liu, D. Wu, X. Feng, L. Wu, *Chem. Eur. J.* **2013**, *19*, 10895.
[28] D. Mecerreyes, *Prog. Polym. Sci.* **2011**, *36*, 1629.
[29] Y. Zhang, Y. Shen, J. Yuan, D. Han, Z. Wang, Q. Zhang, L. Niu, *Angew. Chem. Int. Ed.* **2006**, *45*, 5867.
[30] S. Baldelli, J. Bao, W. Wu, S.-S. Pei, *Chem. Phys. Lett.* **2011**, *516*, 171.
[31] J. L. Bideau, L. Viau, A. Vioux, *Chem. Soc. Rev.* **2011**, *40*, 907.
[32] D. E. Katsoulis, *Chem. Rev.* **1998**, *98*, 359.
[33] M. H. Yang, B. G. Choi, H. Park, W. H. Hong, S. Y. Lee, T. J. Park, *Electroanalysis* **2010**, *22*, 1223.

[34] D. Pan, J. Chen, W. Tao, L. Nie, S. Yao, *Langmuir* **2006**, *22*, 5872.
[35] R. B. King, *Inorg. Chem.* **1991**, *30*, 4437.
[36] M. A. Schwegler, P. Vinke, M. V. D. Eijk, H. V. Bekkum, *Appl. Catal. A* **1992**, *80*, 41.
[37] M. Sadakane, E. Steckhan, *Chem. Rev.* **1998**, *98*, 219.
[38] A. M. White, R. C. T. Slade, *Synth. Met.* **2003**, *139*, 123.
[39] A. K. Cuentas-Gallegos, R. Martínez-Rosales, M. Baibarac, P. Gómez-Romero, M. E. Rincón, *Electrochem. Commun.* **2007**, *9*, 2088.
[40] M. Ammam, J. Fransaer, *J. Electrochem. Soc.* **2011**, *158*, A14.
[41] J. Suárez-Guevara, V. Ruiz, P. Gomez-Romero, *J. Mater. Chem. A* **2014**, *2*, 1014.
[42] G. Román-Pérez, J. M. Soler, *Phys. Rev. Lett.* **2009**, *103*, 096102.
[43] J. Klimeš, D. R. Bowler, A. Michaelides, *Phys. Rev. B* **2011**, *83*, 195131.
[44] P. L. Taberna, P. Simon, J. F. Fauvarque, *J. Electrochem. Soc.* **2003**, *150*, A292.
[45] X.-D. Mu, J.-Q. Meng, Z.-C. Li, Y. Kou, *J. Am. Chem. Soc.* **2005**, *127*, 9694.
[46] X. Zhou, T. Wu, K. Ding, B. Hu, M. Hou, B. Han, *Chem. Commun.* **2010**, *46*, 386.
[47] W. S. Hummers, R. E. Offeman, *J. Am. Chem. Soc.* **1958**, *80*, 1339.
[48] D. Qu, H. Shi, *J. Power Sources* **1998**, *74*, 99.
[49] G. Kresse, J. Furthmüller, *Phys. Rev. B* **1996**, *54*, 11169.
[50] J. P. Perdew, K. Burke, M. Ernzerhof, *Phys. Rev. Lett.* **1996**, *77*, 3865.
[51] Y. Zhang, W. Yang, *Phys. Rev. Lett.* **1998**, *80*, 890.
[52] P. E. Blöchl, *Phys. Rev. B* **1994**, *50*, 17953.
[53] S. Ganapathy, M. Fournier, J. F. Paul, L. Delevoye, M. Guelton, J. P. Amoureux, *J. Am. Chem. Soc.* **2002**, *124*, 7821.